CHEMISTRY OF MATERIALS

pubs.acs.org/cm Article

Increasing Capacity in Disordered Rocksalt Cathodes by Mg Doping

Peichen Zhong,[‖] Zijian Cai,[‖] Yaqian Zhang, Raynald Giovine, Bin Ouyang, Guobo Zeng, Yu Chen, Raphaële Clément, Zhengyan Lun,* and Gerbrand Ceder*

Cite This: https://dx.doi.org/10.1021/acs.chemmater.0c04109 Read Online

ACCESS | Metrics & More | Article Recommendations | Supporting Information

ABSTRACT: Using both computations and experiments, we demonstrate that the performance of Li-excess cation-disordered rocksalt cathodes can be improved by Mg substitution. Mg reduces the amount of Li in the compound that is strongly bound to F and thereby increases the capacity. This enables the use of fluorination as a tool to improve stability of the compounds without significant loss of capacity. Mg emerged as the most optimal substitution element from a systematic computational study aimed at identifying inactive doping elements with a strong enough bonding strength to fluorine to displace Li from the F environments. Our results also show that capacity can be traded for cycle life depending on whether Mg is substituted for Li or for the redox metal. This design strategy should be considered in fluorinated cathodes, which will facilitate the design of optimized disordered rocksalt oxyfluoride cathodes.

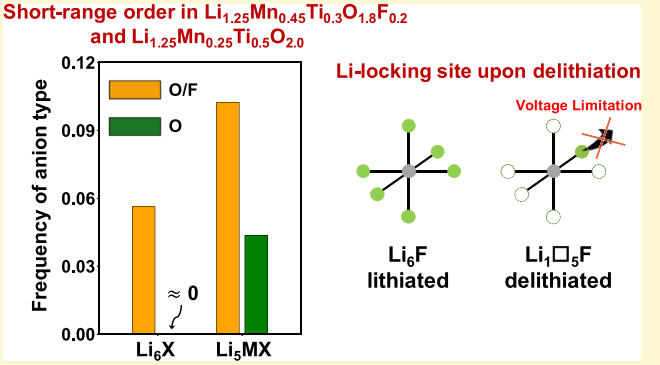

Downloaded via LAWRENCE BERKELEY NATL LABORATORY on December 3, 2020 at 19:46:21 (UTC).
See https://pubs.acs.org/sharingguidelines for options on how to legitimately share published articles.

INTRODUCTION

The continued growth of the Li-ion battery industry depends on the discovery of high-energy-density cathode materials based on nonprecious elements.[1] Conventionally, Li-(Ni,Mn,Co)O_2 (NMC) class cathode materials composed of the redox active elements Ni and Co and the stabilizer Mn^{4+} are mostly used in the industry.[2] Recently, facile Li transport has also been demonstrated in cation disordered rocksalt (DRX) cathode materials, where Li-ion diffusion occurs via a percolating network of Li-rich environments.[3] As these materials do not require the cation chemistry to favor any particular ordering, they can be synthesized with a wide variety of metals.[4] Figure 1a presents the typical DRX crystal structure with interpenetrating cation and anion face-centered cubic (fcc) sublattices. In DRX materials, Li ions diffuse between neighboring octahedral (O_h) sites via an intermediate tetrahedral (T_d) site, as illustrated in Figure 1a. A 0-TM channel is formed when no transition metal (TM) surrounds the T_d site. This 0-TM channel has a low lithium migration barrier energy compared to other types of clusters and is thus beneficial for Li-ion transport.[3] When sufficient Li-excess is present in a compound, 0-TM channels can be long-range connected, enabling percolation. Lee et al.[3] showed that a certain amount of Li-excess ($Li_{1+x>1.09}$ in case of randomly distributed cations) is required to enable Li percolation in a $Li_{1+x}TM_{1-x}O_2$. The percolating Li content can be used as a metric to evaluate the Li capacity of DRX cathodes.

However, the higher Li content in DRX cathodes results in a decrease in available TM redox, and increased reliance on oxygen redox, which is detrimental to long-term capacity retention.[5−8] Hence, a key objective in the DRX cathode design is to maximize the TM redox capacity while maintaining a high level of Li-excess. Fluorination of Li-TM oxides is one such strategy as it can lead to increased capacity by reducing the TM valence in the discharged state.[9−12] In addition, fluorine substitution has been found to protect the surface of DRX particles.[13,14] While the solubility of fluorine in a layered $LiTMO_2$ phase is extremely low, fluorine substitution is thermodynamically favorable in the DRX phase, due to the statistical occurrence of anion environments predominantly coordinated by Li.[15] Using density functional theory (DFT) and solid-state nuclear magnetic resonance (ss-NMR) spectroscopy, Clément et al.[16] demonstrated the existence of Li−F short-range order (SRO) and its coupling to unusual modes of nickel redox in DRX cathodes. More recently, Mozhzhukhina et al.[17] confirmed the existence of Li−F SRO by Raman spectroscopy. Lun et al.[18] argued that the degree of fluorination has a significant impact on the cathode material design by improving the Li percolating network and thus achieving faster ionic diffusion. In addition, Ouyang et al.[19] recently showed that fluorination can substantially affect SRO and, at sufficiently high concentrations, is beneficial to Li-ion transport.

Received: October 21, 2020
Revised: November 22, 2020

© XXXX American Chemical Society

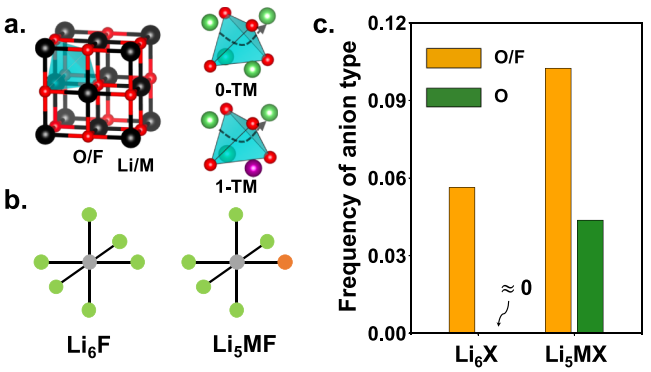

Figure 1. (a) Crystal structure of DRX cathodes. The black spheres represent metal cations (including lithium, TM, and doping metal), and the red spheres represent anions (including oxygen and fluorine). Both cations and anions are in octahedral coordination (O_h). The blue tetrahedral site (T_d) is an intermediate site on the pathway that Li takes when it migrates between two octahedral sites. The 0-TM and 1-TM tetrahedrons are illustrated. (b) Schematic illustration of two frequently occurring cation configurations [Li_6X and Li_5MX (X = anion) around a fluorine atom]. (c) Frequency of configuration Li_6X and Li_5MX in simulated pure oxide and oxyfluoride compounds. The orange and green bars represent the fluorinated and unfluorinated composition of $Li_{1.25}Mn_{0.45}Ti_{0.3}O_{1.8}F_{0.2}$ and $Li_{1.25}Mn_{0.25}Ti_{0.5}O_{2.0}$, respectively.

Though fluorination brings several performance improvements to DRX materials, Li−F SRO also has some negative effects on the capacity and energy density of DRX cathodes. One problem in Li-TM oxyfluorides is the Li−F "locking effect." This effect manifests itself as a high voltage required to extract all Li ions from the Li-rich environment that coordinates with F (Figure 1b). Using DFT calculations, Kitchaev et al.[20] reported that the voltage is greater than 5.0 V to extract the Li from a fluorine coordination shell and makes the fluorine uncoordinated. The voltage is well above the typical electrolyte stability limit, which means a fraction of Li is "locked" to fluorine. To illustrate the significance of the Li locking effect in oxyfluorides, we show in Figure 1c the frequency with which Li_6X and Li_5MX (X = anion) environments are found in $Li_{1.25}Mn_{0.45}Ti_{0.3}O_{1.8}F_{0.2}$ and $Li_{1.25}Mn_{0.25}Ti_{0.5}O_{2.0}$. These results were obtained by averaging over structures obtained from Monte Carlo (MC) simulations at 1000 °C, using a cluster expansion (CE) Hamiltonian parameterized by DFT. In Figure 1c, the orange and green bars represent the oxyfluoride and pure oxide compounds, respectively. The frequency with which these two types of anion environments occur in oxyfluorides are much higher than in pure oxides; in particular, the presence of Li_6X is almost never found in the oxide but occurs frequently in the oxyfluoride. At least one Li ion is impossible to be extracted from the Li_6F environment, which limits "extractable lithium" capacity.[20] Thus, to achieve higher capacity and energy density, one of the key factors is to reduce the number of "locked" lithium ions around fluorine.

Here, we offer a solution to this issue, which consists of adding another inactive cation that displaces some Li from the F environments to an environment from which it can be extracted. This requires a cation with similar or stronger F-bonding preference and similar ionic radius to Li. As the doped cation is not extractable, it also prevents the formation of under-coordinated fluorine after the removal of Li ions. In this study, we first screen various main group elements in terms of (1) bonding energies in metal fluorides and (2) ionic radius difference with Li^+, selecting species that are comparable to lithium. The results indicate that magnesium (Mg) satisfies both criteria and is a promising element to substitute to fluorinated DRX materials. A detailed theoretical investigation of Li−F SRO using DFT calculations and CE MC simulations confirms that Mg doping results in a greater fraction of extractable Li ions by reducing the frequency of the Li_6F configuration. We verify our hypothesis by characterizing the structure of $Li_{1.25}Mn_{0.45}Ti_{0.3}O_{1.8}F_{0.2}$ and $Li_{1.25}Mg_{0.1}Mn_{0.45}Nb_{0.2}O_{1.8}F_{0.2}$ and evaluating the electrochemical performance. Though both compounds have the same Li-excess and Mn content, the Mg-doped compound has higher capacity. Finally, we extend the discussion to a related group of compositions: $Li_{1.333}Mn_{0.667}O_{1.333}F_{0.667}$ (LMF), $Li_{1.233}Mg_{0.1}Mn_{0.667}O_{1.333}F_{0.667}$ (ls-LMF), $Li_{1.333}Mg_{0.1}Mn_{0.567}O_{1.333}F_{0.667}$ (ms-LMF), and $Li_{1.28}Mg_{0.11}Mn_{0.61}O_{1.333}F_{0.667}$ (LMMF) to demonstrate that the improved Li use, enabled by Mg doping, can also be traded to improve cycle life.

METHODS

Computational Methods. To evaluate the equilibrium ordering of multicomponent DRX compounds, we constructed a CE Hamiltonian in the configurational space LiF−MgO−$LiMnO_2$, LiF−MgO−$LiMnO_2$−Li_3NbO_4, and LiF−$LiMnO_2$−Li_2TiO_3 on a rocksalt lattice. The CE technique is used to study the configurational thermodynamics of materials featuring a mixture of species on cation sites and has been applied to study Li-vacancy configurations in layered materials.[21] As in the LiF−$LiMnO_2$−Li_2TiO_3 system, the anion fcc lattice comprises O^{2-} and F^-, while the lattice of octahedral cation is composed of Li^+, Mn^{3+}, and Ti^{4+}/Nb^{5+}. A coupled sublattice approach was therefore used.[22] We fitted a CE model consisting of pair interactions up to 7.1 Å, triplet interactions up to 4.0 Å, and quadruplet interactions up to 4.0 Å based on a primitive cell of the rocksalt structure with a lattice parameter a = 3 Å. Effective cluster interactions were obtained from l_1-norm regularized linear regressions with the best regularization parameter selected to minimize the cross-validation (CV) score.[23,24] The root-mean squared CV errors were converged to below 8 meV/atom.

All DFT calculations were performed with the Vienna Ab initio Simulation Package[25] using the projector-augmented wave method,[26] a plane-wave basis set with an energy cutoff equal to 520 eV, and a reciprocal space discretization of 25 k-points per Å. All calculations were converged to 10^{-6} eV in total energy for electronic loops and 0.02 eV/Å in interatomic forces for ionic loops. We used the Perdew−Burke−Ernzerhof generalized gradient approximation exchange−correlation functional[27] with rotationally averaged Hubbard U correction (GGA + U) to compensate for the self-interaction error on all TM atoms except titanium.[28] The U parameters were obtained from the literature, where they were calibrated to TM oxide formation energies (3.9 eV for Mn and 1.5 eV for Nb). The GGA + U computational framework is believed to be reliable in determining the formation enthalpies of similar compounds.[29]

MC simulations on these CE Hamiltonians were performed in a canonical ensemble using Metropolis-Hastings sampling on a 8 × 8 × 10 supercell (1280 atoms) of the primitive unit cell of the rocksalt structure. All statistical quantities were obtained from 1000 sampled structures of the equilibrium ensemble. Percolation analysis was completed on these sampled structures using the dribble package.[3]

Synthesis. $Li_{1.25}Mn_{0.45}Ti_{0.3}O_{1.8}F_{0.2}$ (LMTF) and $Li_{1.25}Mg_{0.1}Mn_{0.45}Nb_{0.2}O_{1.8}F_{0.2}$ (LMMNF) were synthesized by the solid-state reaction. Li_2CO_3 (Alfa Aesar, ACS, 99%), Mn_2O_3 (Alfa Aesar, 98%), TiO_2 (Anatase, Alfa Aesar, 99.9%), Nb_2O_5 (Alfa Aesar, 99.9%), MgF_2 (Alfa Aesar, 99.9%), and LiF (Alfa Aesar, 99.99%) were used as precursors. The precursors were stoichiometrically dispersed into ethanol in a 50 mL stainless-steel jar with five 10 mm (diameter)

https://dx.doi.org/10.1021/acs.chemmater.0c04109
Chem. Mater. XXXX, XXX, XXX−XXX

stainless-steel balls (except that 10% excess Li_2CO_3 was added to compensate for possible loss during synthesis). After ball milling at 250 rpm for 12 h, the precursors were dried overnight in an oven. The mixture of the precursors was pelletized and then sintered at 600 °C for 2 h in Ar to decompose the carbonates, followed by calcining at 1000 °C for 4 h in Ar. The pellet was transferred to a glovebox after furnace cooling to room temperature. After calcination, the pellets were manually ground into fine powder.

$Li_{1.333}Mn_{0.667}O_{1.333}F_{0.667}$ (LMF), $Li_{1.28}Mg_{0.11}Mn_{0.61}O_{1.333}F_{0.667}$ (LMMF), $Li_{1.333}Mg_{0.1}Mn_{0.567}O_{1.333}F_{0.667}$ (ms-LMF), and $Li_{1.233}Mg_{0.1}Mn_{0.567}O_{1.333}F_{0.667}$ (ls-LMF) were synthesized by mechanochemical ball milling. Li_2O (Alfa Aesar, ACS, 99%), MgF_2 (Alfa Aesar, 99.9%), MnO (Sigma-Aldrich, 99.99%), Mn_2O_3 (Alfa Aesar, 99%), MnO_2 (Alfa Aesar, 99.9%), and LiF (Alfa Aesar, 99.99%) were stoichiometrically added into a 50 mL stainless-steel jar with five 10 mm (diameter) and ten 5 mm (diameter) stainless-steel balls. The total amount of precursors was 1 g. The jars were sealed with a safety closure in an Ar-filled glovebox after ball milling at 500 rpm for 40, 40, 35, and 35 h for LMF, LMMF, ms-LMF, and ls-LMF, respectively.

Electrochemistry. To prepare a cathode film for each material, 210 mg of active material and 60 mg of Super C65 carbon black were mixed and shaker-milled for 1 h in an Ar atmosphere using a SPEX 800M Mixer/Mill. Then, 90 mg of the mixture was manually mixed with 10 mg of polytetrafluoroethylene and rolled into a thin film in a glovebox. Coin cells (CR2032) were assembled by using commercial 1 M $LiPF_6$ in ethylene carbonate and dimethyl carbonate solution (volume ratio 1:1) as the electrolyte, glass microfiber filters (Whatman) as separators, and Li metal foil (FMC) as the anode. The coin cells were tested on an Arbin battery cycler at room temperature. The loading density of the cathode films was approximately 3 mg/cm^2 based on the active materials.

Compositional, Structural, and Morphological Characterization. X-ray diffraction (XRD) patterns of the as-synthesized compounds were obtained using a Rigaku MiniFlex diffractometer (Cu source) in the 2θ range of 5−85°. Rietveld refinement was performed using PANalytical X'pert HighScore Plus software. Scanning electron microscopy (SEM) images were obtained using a Zeiss Gemini Ultra-55 analytical field-emission scanning electron microscope at the Molecular Foundry at Lawrence Berkeley National Lab (LBNL). High-angle annular dark-field scanning transmission electron microscopy (HAADF-STEM) and energy-dispersive X-ray spectroscopy (EDX) mapping were performed on a FEI TitanX 60−300 microscope equipped with a Bruker windowless EDX detector at an acceleration voltage of 200 kV at the Molecular Foundry at LBNL.

Solid-State Nuclear Magnetic Resonance. ^{19}F NMR data of LMTF, LMMNF, LMF, and LMMF were recorded at B_0 = 7.05 T (300 MHz for ^1H) on a super wide bore Bruker BioSpin spectrometer equipped with an AVANCE-III console. Spectra were obtained with a 2.5 mm double-resonance HX magic angle spinning (MAS) probe tuned to ^{19}F (282.4 MHz), spinning at ν_R = 30 kHz. Chemical shifts were externally referenced against pure lithium fluoride powder [LiF, $\delta_{iso}(^{19}F)$ = 204 ppm].

Due to the wide frequency range covered by ^{19}F resonances in LMTF, LMMNF, LMF, and LMMF, it is impossible to excite the entire ^{19}F NMR spectrum with a single radio frequency (RF) pulse. Instead, nine spin echo sub-spectra were recorded, with the irradiation frequency varied in steps of 425 ppm or 120 kHz from −1700 to 1700 ppm, and these sub-spectra were added together to obtain the final sum spectrum for each sample. For this, each individual sub-spectrum was processed using a zero-order phase correction so that the on-resonance signals are in the adsorption mode. The nine sub-spectra were then added together to give an overall sum spectrum with no further phase correction required. This "frequency stepping,"[30,31] "spin echo mapping,"[32] or "variable offset cumulative spectrum"[33] methodology provides a large excitation bandwidth with uniform excitation of the broad ^{19}F signals. Individual ^{19}F rotor-synchronized spin echo spectra ($90° - \tau R - 180° - \tau_R$) were obtained using 90° and 180° RF pulses of 0.7 and 1.4 μs at 200 W, respectively, and 10,240 scans collected using a 30 ms recycle delay.

RESULTS

Screening Results. The M−F bonding energy is calculated from the formation enthalpy per F atom, $\Delta H_f/y$, of the metal fluoride MF_y. The values of $\Delta H_f/y$, where ΔH_f is obtained from the Materials Project,[34] are shown in Figure 2. As a baseline, the bonding energy of Li per F is −3.18 eV. No other element has stronger bonding with F than Li. The fluorides of the {Sc, Y} and {B, Al, Ga} groups have less negative enthalpy than the {Be, Mg, Ca} group. Thus, only group-II elements have comparable interaction with F to Li.

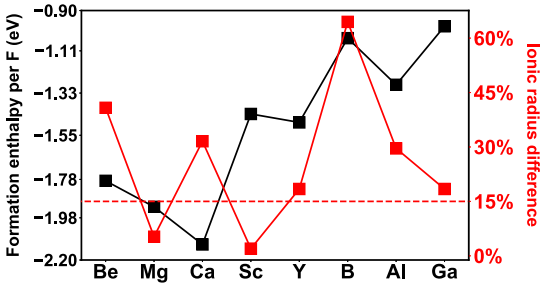

Figure 2. Screening of main group elements on bonding preference with F and ionic size difference with Li. The black and red lines represent formation enthalpy per F and percentage of ionic radius difference with Li ion, respectively. The dashed red line corresponds to a 15% radius difference.

Another criterion is the ability to accommodate the dopant in the DRX structure. Empirically, the Hume−Rothery rule predicts that species with similar electronegativity form a solid solution when their atomic radii differ by no more than 15%.[35] Even though this criterion is determined for metallic alloys, we adopt it here to determine whether a candidate element might be substituted in the cation-disordered phase. In Figure 2, the red squares represent the percentage of ionic radii difference with Li^+, and the red dashed line represents 15% difference.[36] Only Mg^{2+} and Sc^{3+} satisfy this criterion, although Y^{3+} and Ga^{3+} are only slightly above the 15% line. Combining the radius information with the energetic preferences points at Mg^{2+} being a suitable cation.

Computational Predictions. To characterize in more detail how Mg addition affects cation ordering and Li−F SRO in DRX materials, we computationally investigated two compounds, $Li_{1.25}Mn_{0.45}Ti_{0.3}O_{1.8}F_{0.2}$ (LMTF) and $Li_{1.25}Mg_{0.1}Mn_{0.45}Nb_{0.2}O_{1.8}F_{0.2}$ (LMMNF) with identical Li-excess, redox active TM, and fluorination amount. Canonical CEMC simulation was applied at 1000 °C to simulate the as-synthesized samples.[20] The frequency of different cation configurations around F and their percolation properties were averaged over 1000 structures sampled from the equilibrium ensemble.

Figure 3a shows the frequency with which several types of cation environments around F occur. The Li_6F and Li_5MF environments dominate both LMTF and LMMNF. In LMTF, without Mg-doping, over 50% of F ions are surrounded by six Li ions. However, the peak of the distribution shifts to Li_5MF in LMMNF, and the Li_6F frequency is lowered to 35%. In particular, the $LiMg_5F$ environment, shown as the brown dashed bar, makes up around 37% of the Li_5MF environments. This finding indicates that modifying the DRX composition with Mg can effectively reduce the number of Li_6F environments and render Li ions more accessible.

https://dx.doi.org/10.1021/acs.chemmater.0c04109
Chem. Mater. XXXX, XXX, XXX−XXX

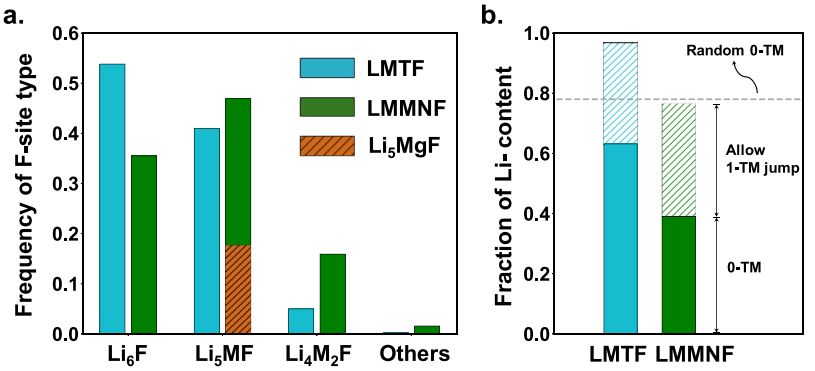

Figure 3. (a) Frequency of different types of fluorine environments averaged over 1000 sampled structures from the equilibrium ensemble. LMTF/LMMNF is represented by the blue/green bar, respectively. The brown dashed bar represents the $LiMg_5F$ environment in LMMNF. (b) Percolation analysis of LMTF and LMMNF. The solid bar represents percolating Li-content in the 0-TM percolating network, and the dashed bar (1-TM) represents additional percolating Li-content when one jump through a 1-TM barrier into the 0-TM network is included.

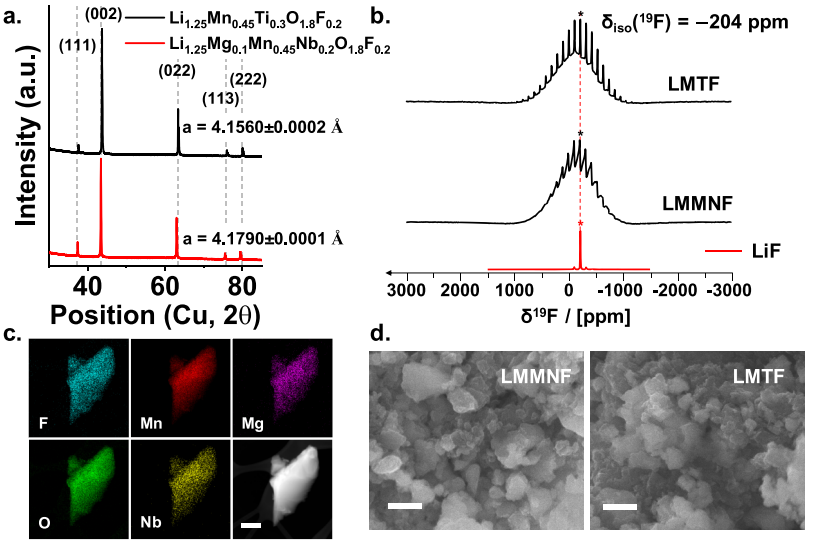

Figure 4. Structural and morphological characterization of LMTF and LMMNF. (a) XRD patterns of LMTF and LMMNF indexed according to the rocksalt structure. (b) ^{19}F spin echo MAS NMR spectra of LMTF and LMMNF recorded at B_0 = 7.05 T. For comparison, ^{19}F spin echo spectra collected under similar experimental conditions on a LiF powder sample are shown in red. The isotropic shift of the sharp resonance corresponding to ^{19}F nuclei in LiF-like environments in the ^{19}F NMR spectra is denoted with an asterisk. Spinning sidebands due to fast rotation of the samples during data acquisition are observed on either side of the isotropic signals. (c) TEM−EDS mapping of the element distribution in a representative particle of as-synthesized LMMNF (scale bar: 300 nm). (d) SEM images of as-synthesized LMTF and LMMNF (scale bar: 400 nm).

LMTF and LMMNF also differ in their d^0 charge compensating element. Although Ti^{4+} and Nb^{5+} are both electrochemical inactive, they can affect atomic ordering and thus the percolating Li content of DRX cathodes.[37,38] To rule out that the capacity improvement of LMMNF is caused by the change in the charge compensator, the fraction of the Li content in the percolating network of each compound is plotted in Figure 3b. The gray dashed line indicates that a percolating Li content of approximately 78% is achieved when the cations are randomly arranged. The solid bar represents the fraction of the Li content in the 0-TM network, and the dashed bar represents the Li that can reach the 0-TM network with a single 1-TM hop. LMTF has a higher fraction of the Li content in both the 0-TM and 1-TM networks, as compared to LMMNF. These results are consistent with percolation predictions in the previous work[39] on Li-TM oxides. Thus, the larger fraction of accessible Li ions in LMMNF more likely originates from the fact that Mg displaces Li from the F-bonded position than from the percolating Li content. Compared with LMTF, Mg-doped LMMNF has a much lower frequency of Li_6F environments, leading us to predict a higher achievable electrochemical capacity for LMMNF than that for LMTF.

Experimental Verification. LMTF and LMMNF were synthesized, as described in the Methods section. The XRD pattern (Figure 4a) indicates that both materials form a DRX structure (space group: $Fm\bar{3}m$) without any detectable impurity phases. The Rietveld refinement reveals a simple DRX structure (see Supporting Information, Figure S1) and gives a lattice parameter of 4.1560 Å (LMTF) and 4.1790 Å (LMMNF). As the only change from LMTF to LMMNF is the substitution of Ti^{4+} (74.5 pm) by Mg^{2+} (86 pm) and Nb^{5+} (78 pm), the increase in the lattice parameter is expected.

HAADF-STEM images and the corresponding EDX elemental mapping of LMTF and LMMNF are presented in Figures S2 and 4c, respectively. The elemental mapping of LMTF and LMMNF reveals that all elements are homogeneously distributed in representative particles, without surface

https://dx.doi.org/10.1021/acs.chemmater.0c04109
Chem. Mater. XXXX, XXX, XXX−XXX

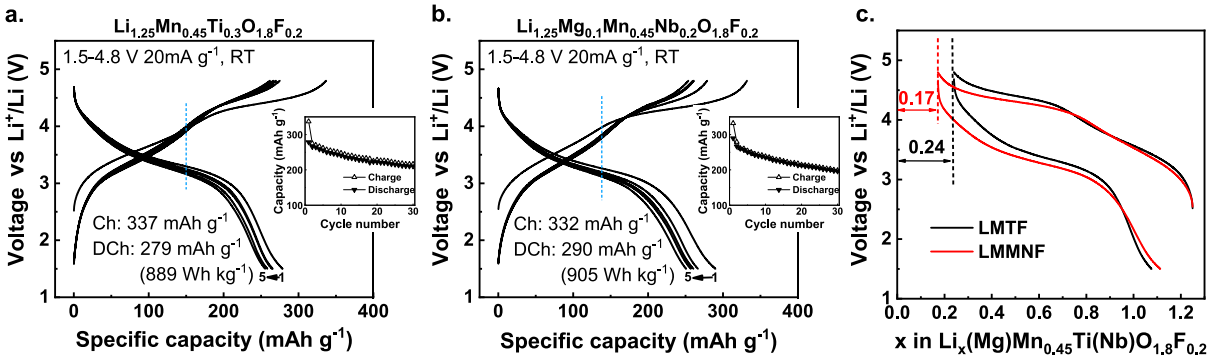

Figure 5. Voltage profiles of the first five cycles and capacity retention of (a) LMTF and (b) LMMNF within a voltage window of 1.5−4.8 V at 20 mA g^{-1} at room temperature. The initial charge and discharge capacity and energy density are shown in the figure. (c) Direct comparison of extractable Li ions in LMTF and LMMNF in the electrochemical test. The amount of remaining Li content is 0.24/0.17 per f.u. at the top of charge for LMTF/LMMNF, respectively.

segregation or phase separation, indicating that Mg and F are successfully incorporated into the bulk. SEM images shown in Figure 4d indicate an average primary particle size of ∼ 400−500 nm for both LMTF and LMMNF samples. The agglomeration of primary particles into secondary particles around ∼ 1 μm in size is observed.

^{19}F ss-NMR measurements were conducted to verify the bulk integration of F. The ^{19}F NMR spectra obtained on LMTF and LMMNF (Figure 4b) exhibit a broad signal, spanning more than 2000 ppm, overlapping with a sharp signal comprising a centerband at the isotropic shift (−204 ppm, indicated with an asterisk) and a series of sidebands on either side of the centerband resulting from fast spinning of the sample during data acquisition. The broad signal comprises several broad and overlapping signals characteristic of ^{19}F nuclei incorporated into the bulk DRX structural framework, as reported for related systems.[4,9,16,40,41] This broad signal corresponds to ^{19}F nuclei in the bulk of the material, which is the result of (i) a distribution of chemical shifts due to the large number of F local environments in the cation-disordered structure and (ii) NMR line broadening caused by strong paramagnetic interactions between F nuclei and nearby unpaired *d* electrons on Mn ions within the DRX structure. The sharp signal at −204 ppm resonates at the same frequency as ^{19}F nuclei in pure LiF (spectrum shown in red in Figure 4b) and is therefore attributed to ^{19}F nuclei in LiF-like diamagnetic environments. LiF-like ^{19}F signals in the spectra collected on DRX samples exhibit many more sidebands than the pure LiF signal collected under similar conditions. The greater number of sidebands signifies an increase in the chemical shift anisotropy of ^{19}F nuclei in LiF-like environments in the DRX samples, resulting from their close proximity to Mn centers and long-range anisotropic paramagnetic interactions. These observations suggest that LiF-like ^{19}F environments either arise from Li-rich F local environments in the rocksalt cathodes or from a thin layer of LiF the rocksalt impurity phase at the surface of the DRX particles. It is important to note that when F is directly bonded to a Mn ion, the paramagnetic interaction becomes so strong that the resulting NMR signal is too broad and too short lived to be detected.[16] Hence, the amount of impurity LiF cannot be determined quantitatively from ^{19}F NMR as part of the signal from the DRX cathode is missing. Assuming that a diamagnetic LiF impurity phase is present, the intensity ratio of the broad paramagnetic signal to the sharp diamagnetic signal (para/dia) still indicates that the great majority of F ions are incorporated into the bulk of both LMTF and LMMNF compounds.

In Figure 5, the electrochemical properties of LMTF and LMMNF are compared using galvanostatic cycling between 1.5 and 4.8 V at 20 mA g^{-1} and room temperature. The blue dashed lines represent the theoretical capacity based on $Mn^{3+/4+}$ redox in each sample. LMTF delivered a first charge capacity of 337 mAh g^{-1} and a discharge capacity of 279 mAh g^{-1} (899 Wh kg^{-1}). LMMNF delivered a similar initial charge capacity of 332 mAh g^{-1} but a larger discharge capacity of 290 mAh g^{-1} (905 Wh kg^{-1}). Charging extracted 1.01 Li and 1.08 Li per formula unit (f.u.) from LMTF and LMMNF, respectively. The locked Li content decreases by about 29% from 0.24 per f.u. in LMTF to 0.17 per f.u. in LMMNF with the substitution of Ti by Mg and Nb, as shown in Figure 5c. To verify that this improvement is not caused by the change in chemistry of the charge-compensating element, $Li_{1.25}Mn_{0.6}Nb_{0.15}O_{1.8}F_{0.2}$ (LMNF) was synthesized and compared with LMMNF. LMNF exhibits a lower initial charge capacity of 293 mAh g^{-1}, as compared to LMMNF (Figure S3), and the amount of nonextractable Li at top of the charge is increased to 0.28 per f.u. in unsubstituted LMNF. Therefore, the decrease of locked Li is not caused by the change of high-valent charge compensators.

Extended Study on Li/TM Substitution. To further illustrate the validity of the Mg-doping strategy and critically examine the Mg-doping effect without the effect of different d^0 TM charge compensators, we further studied the composition $Li_{1.333}Mn_{0.667}O_{1.333}F_{0.667}$ (LMF),[18,42] which shows lower capacity but better capacity retention than the related disordered Li_2MnO_3. LMF delivers a first charge and discharge capacity of 276 and 267 mAh g^{-1} (Figure S4a), respectively, which is lower than that in disordered Li_2MnO_3.[43] This comparison is consistent with our understanding of the role that F plays: its locking effect reduces capacity, but it also mitigates the irreversible oxygen redox process and reduces oxygen loss, which improves cycling. Mg can be introduced in a variety of ways into DRX compounds depending on how charge compensation is achieved. Using the Li−Mn−O−F system as an example, we show below that this degree of freedom can be used to tune the initial capacity versus cyclability, which is summarized in Table 1. In the previous example, Mg was incorporated by substituting Ti with a charge−equivalent combination of Mg and Nb. Other strategies would be to (1) substitute Mn with Mg, leading to

https://dx.doi.org/10.1021/acs.chemmater.0c04109
Chem. Mater. XXXX, XXX, XXX−XXX

Table 1. Notation of all Compositions Chosen in This Study[a]

notation	composition	note
LMTF	$Li_{1.25}Mn_{0.45}Ti_{0.3}O_{1.8}F_{0.2}$	solid-state synthesis, low F content
LMMNF	$Li_{1.25}Mg_{0.1}Mn_{0.45}Nb_{0.2}O_{1.8}F_{0.2}$	$Ti_{0.3}$ to $Mg_{0.1}Nb_{0.2}$ by charge-balanced substitution
LMF	$Li_{1.333}Mn_{0.667}O_{1.333}F_{0.667}$	ball-milling synthesis, high F content
ls-LMF	$Li_{1.233}Mg_{0.1}Mn_{0.667}O_{1.333}F_{0.667}$	Li to Mg substitution, O redox ↓, retention ↑
ms-LMF	$Li_{1.333}Mg_{0.1}Mn_{0.567}O_{1.333}F_{0.667}$	Mn to Mg substitution, extractable Li ↑, capacity ↑
LMMF	$Li_{1.28}Mg_{0.11}Mn_{0.61}O_{1.333}F_{0.667}$	mixed substitution, all Mn^{3+}, nonextractable Li ↓

[a]In each case, the compositional design objective is briefly described in the note.

a higher Mn valence and constant Li-excess level and (2) substitute Li with Mg, leading to a lower Mn valence and Li-excess level. To test both strategies, $Li_{1.333}Mg_{0.1}Mn_{0.567}O_{1.333}F_{0.667}$ (ms-LMF) and $Li_{1.233}Mg_{0.1}Mn_{0.667}O_{1.333}F_{0.667}$ (ls-LMF) were prepared by mechanochemical ball milling. The notation ms-LMF refers to the sample where Mn was substituted by Mg, and the notation ls-LMF refers to the sample where Li was substituted by Mg. To exclude the particle size effect on the electrochemical performance, SEM was conducted and these images are shown in Figure S5.

As the Li-excess content remains high in ms-LMF, Mg can free the locked Li to achieve a larger capacity. In agreement with this prediction, ms-LMF exhibits an initial charge (and discharge) capacity of 305 (and 309 mAh g^{-1}), which is larger than that for LMF (Figure S4). Through this substitution strategy, a specific discharge energy of 1001 Wh kg^{-1} can be achieved. With more capacity contribution from anionic redox, a capacity of 252 mAh g^{-1} is retained (81.6% of the initial capacity) compared to that of LMF (226 mAh g^{-1}, 84.3%) over 30 cycles (Figure 6b).

In contrast, a lower capacity is expected in ls-LMF as it lowers the Li-excess level. Indeed, it delivers initial charge and discharge capacities of 271 and 260 mAh g^{-1} (a specific energy of 806 Wh kg^{-1}), respectively (Figure S4b). However, the capacity retention of ls-LMF is improved over LMF (248 mAh g^{-1} after 30 cycles, 91.5% of the initial capacity) presumably as a result of the theoretical TM capacity that is gained from Mn by lowering its valence in the as-synthesized sample, leading to less oxygen redox.

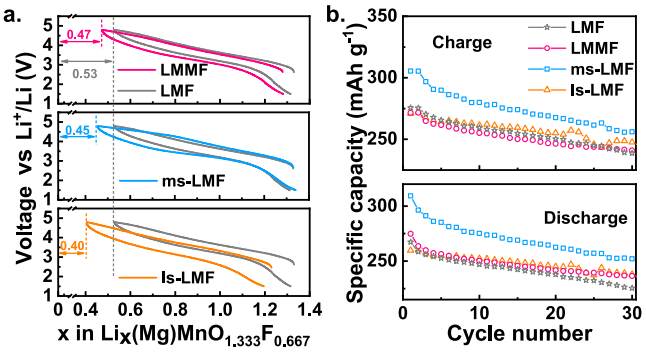

Figure 6. (a) Voltage profiles of ls-LMF, ms-LMF, LMMF, and LMF within a voltage window of 1.5−4.8 V at 20 mA g^{-1} at room temperature. The amount of remaining Li per f.u. at top of charge is shown in the figure. The gray curves represent the first cycle voltage profile of LMF for comparison. (b) Cyclability of all Li−(Mg)−Mn−O−F compounds at 20 mA g^{-1} at room temperature within a voltage window of 1.5−4.8 V.

These results show the two different Mg substitution strategies in fluorinated Li-excess DRX materials, each serving a different purpose: Mg can either substitute for the TM to free some locked Li, resulting in a higher initial capacity with reasonable capacity retention, or Mg can substitute for Li and lower the TM valence, which increases the theoretical TM capacity and results in improved capacity retention. In both cases, the amount of nonextractable Li is lower than that of undoped LMF. This trade off can be influenced by the fluorination level, as shown by Lun et al.[18], a high F content enables one to combine high TM redox capacity with high Li-excess. The comparison of cyclability is also shown in Figure S6.

We also considered co-substitution of Li and Mn by Mg. ^{19}F ss-NMR measurements were once again conducted to confirm the bulk incorporation of F (Figure S7). The voltage profiles of $Li_{1.28}Mg_{0.11}Mn_{0.61}O_{1.333}F_{0.667}$ (LMMF) cycled between 1.5 V and 4.8 V are presented in Figure S4d. LMMF delivered first charge and discharge capacities of 272 and 275 mAh g^{-1}, respectively. Over 30 cycles, a capacity of 236 mAh g^{-1} is retained (85.8% of the initial capacity). The capacity retention of LMMF is intermediate between that of ls-LMF and ms-LMF. Although slightly less charge capacity was delivered compared with LMF (276 mAh g^{-1}), the amount of nonextractable Li at the top of the charge state decreased from 0.53 Li per f.u. for LMF to 0.47 Li per f.u. for LMMF (Figure 6a).

To relate the performance of the co-substituted sample to its structure, a CEMC simulation with temperature 1750 °C as a heuristic limit of the mechanical ball-milling condition was run.[41] The TMs in LMF and LMMF are Mn^{3+} and thus present a similar chemical environment. As shown in Figure 7a, the frequency of the Li_6F configuration is approximately 10% lower in LMMF than in LMF, whereas the frequency of the Li_5MF configuration is quite similar in both compounds. The reduced amount of locked Li in Li_6F indicates that Li ions have been displaced to other nonlocking sites and can thus be effectively extracted within the working voltage window. Considering that the Li-excess amount is different in LMF and LMMF, we introduce a normalized SRO parameter λ to measure the occurrence of Li_6F configuration in the solid solution

$$\lambda = \frac{P_{calc}(Li_6F) - P_{rand}(Li_6F)}{P_{max}(Li_6F) - P_{rand}(Li_6F)} \quad (1)$$

where P_{calc} and P_{rand} represent the calculated and fully random frequency of the Li_6F configuration, respectively. P_{max} is the max probability for Li_6F that can be achieved for the given Li and F content. For all of our samples, $P_{max} = 1$. In Figure 7b, the black solid bar represents the direct frequency of the Li_6F configuration and the dashed bar represents the normalized SRO parameter λ. The frequency by which the Li_6F configuration occurs decreases from 0.41 for LMF to 0.32 for LMMF, and the corresponding SRO parameter λ decreases from 0.35 to 0.28, respectively. Both experimental and computational results confirm that co-substitution of Li/TM with Mg reduces the amount of locked Li.

https://dx.doi.org/10.1021/acs.chemmater.0c04109
Chem. Mater. XXXX, XXX, XXX−XXX

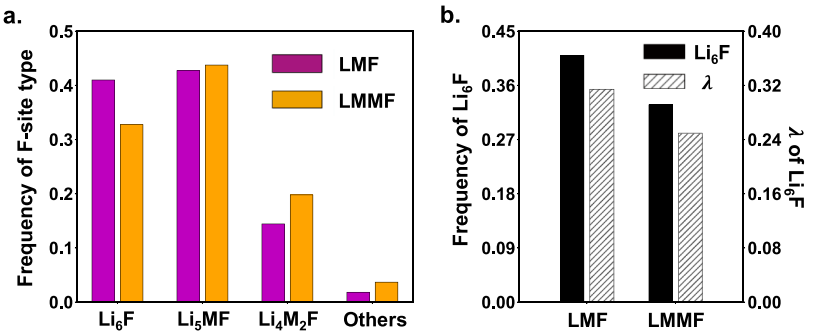

Figure 7. (a) Frequency of different types of fluorine environments averaged 1000 sampled structures from the equilibrium ensemble. (b) Frequency and normalized SRO parameter λ of Li_6F environments of LMF and LMMF.

DISCUSSION

DRX materials require Li-excess to achieve a percolating Li diffusion pathway through a low barrier 0-TM migration channel. At least 9% of excess Li is needed when cations are randomly distributed, while more Li content is needed in practical compounds due to SRO.[18,39] The reduction in electron capacity that this amount of Li-excess causes can be countered by the incorporation of high valent metals and by O to F substitution (which both reduce the TM valence state and increase theoretical TM redox), or by relying on oxygen redox to provide extra electron capacity.[37,44] Fluorine substitution is particularly fruitful as it also seems to stabilize the compounds when they have oxygen redox, leading generally to better capacity retention in many systems.[4,40,45]

From previous work, it is clear that this strategy is not fully optimized. While the Li-excess is needed for percolation, not all Li near F can be extracted motivating our strategy to displace some of it by adding other metal cations. From our computational investigation, we find that Mg is one of the few elements that has the appropriate binding strength with F to displace Li. We show in Figure 5 that when replacing $Ti_{0.3}$ in LMTF with $Mg_{0.1}Nb_{0.2}$ in LMMNF, the nonextractable Li content is reduced by about 30% even though this substitution reduces percolation (Figure 3b). There are other options to compensate for the introduction of Mg in a DRX materials, such as substituting Li/TM with Mg, and our results show that these different substitution strategies can be used to tune either capacity or capacity retention. Substituting Li leads to better capacity retention because the TM average charge valence is reduced and less irreversible oxygen redox is needed. Substituting the TM leads to higher capacity as the Li-excess level is kept constant and Li−F locking is reduced, resulting in a greater fraction of extractable Li. Particularly, we further demonstrated the validity of Mg doping in the LMMF system by substituting Mg for both Li and TM. Without consideration of the Li−F locking effect, LMMF would be expected to deliver lower capacity because of the lower Li and redox active TM content. However, both computational and experimental results indicate that substituting Mg for both Li and TM effectively unlocks more Li by reducing the frequency of Li_6F environments in LMMF, and thus LMMF delivers a comparable charge capacity and higher discharge capacity than LMF. These results unambiguously confirm that it is beneficial to introduce Mg-doping to unlock Li from the Li_6F configuration in DRX oxyfluorides.

From our study of the related group of compositions, the best approach to optimize capacity by incorporation of Mg is to (1) keep the Li-excess amount constant and (2) substitute on the TM (ms-LMF) and/or replace it with a different d^0 charge compensator (LMMNF). This strategy leads to an energy density of 905 and 1001 Wh kg^{-1} in the compound LMMNF (solid-state synthesis approach) and ms-LMF (mechanochemical ball-milling approach), respectively.

CONCLUSIONS

We demonstrated the computational prediction and experimental realization of Mg-doped disordered oxyfluoride cathodes with improved electrochemical performance. Although fluorination enhances the long-term performance of DRX materials, the strong attraction of F to Li can make some of the Li ions that are part of a Li_6F configuration nonextractable within a reasonable voltage window. Our simulations show that the population of Li_6F can be effectively reduced with Mg doping. This is confirmed by experiments on several systematically chosen compositions, successfully demonstrating the validity to unlock Li from the Li_6F configuration. From the study of two groups of compositions, we conclude that the amount of the locked Li content should be considered in oxyfluorides to fully optimize the capacity. Mg^{2+} has an ionic radius similar to that of Li^+ and a strong bonding preference to F, making it a suitable candidate for resolving the Li−F locking effect and increasing the achievable capacity of DRX materials.

ASSOCIATED CONTENT

Supporting Information

The Supporting Information is available free of charge at https://pubs.acs.org/doi/10.1021/acs.chemmater.0c04109.

XRD refinement of all compositions; TEM−EDS mapping of LMTF; electrochemical test of LMNF; electrochemical test, SEM, and cyclability comparison of LMF-based compositions; and ^{19}F NMR of LMF and LMMF (PDF)

AUTHOR INFORMATION

Corresponding Authors

Zhengyan Lun − *Department of Materials Science and Engineering, University of California Berkeley, Berkeley, California 94720, United States; Materials Sciences Division, Lawrence Berkeley National Laboratory, Berkeley, California 94720, United States;* orcid.org/0000-0002-0186-6864; Email: zylun@berkeley.edu

Gerbrand Ceder − *Department of Materials Science and Engineering, University of California Berkeley, Berkeley, California 94720, United States; Materials Sciences Division,*

https://dx.doi.org/10.1021/acs.chemmater.0c04109
Chem. Mater. XXXX, XXX, XXX−XXX

Lawrence Berkeley National Laboratory, Berkeley, California 94720, United States; orcid.org/0000-0001-9275-3605; Email: gceder@berkeley.edu

Authors

Peichen Zhong − *Department of Materials Science and Engineering, University of California Berkeley, Berkeley, California 94720, United States; Materials Sciences Division, Lawrence Berkeley National Laboratory, Berkeley, California 94720, United States;* orcid.org/0000-0003-1921-1628

Zijian Cai − *Department of Materials Science and Engineering, University of California Berkeley, Berkeley, California 94720, United States; Materials Sciences Division, Lawrence Berkeley National Laboratory, Berkeley, California 94720, United States*

Yaqian Zhang − *Department of Materials Science and Engineering, University of California Berkeley, Berkeley, California 94720, United States; Materials Sciences Division, Lawrence Berkeley National Laboratory, Berkeley, California 94720, United States*

Raynald Giovine − *Materials Department, University of California Santa Barbara, Santa Barbara, California 93106, United States*

Bin Ouyang − *Department of Materials Science and Engineering, University of California Berkeley, Berkeley, California 94720, United States; Materials Sciences Division, Lawrence Berkeley National Laboratory, Berkeley, California 94720, United States;* orcid.org/0000-0002-8181-6815

Guobo Zeng − *Department of Materials Science and Engineering, University of California Berkeley, Berkeley, California 94720, United States; Materials Sciences Division, Lawrence Berkeley National Laboratory, Berkeley, California 94720, United States*

Yu Chen − *Department of Materials Science and Engineering, University of California Berkeley, Berkeley, California 94720, United States; Materials Sciences Division, Lawrence Berkeley National Laboratory, Berkeley, California 94720, United States*

Raphaël Clément − *Materials Department, University of California Santa Barbara, Santa Barbara, California 93106, United States;* orcid.org/0000-0002-3611-1162

Complete contact information is available at: https://pubs.acs.org/10.1021/acs.chemmater.0c04109

Author Contributions

‖P.Z. and Z.C. contributed equally.

Notes

The authors declare no competing financial interest.

■ ACKNOWLEDGMENTS

This work was supported by Umicore Specialty Oxides and Chemicals, the Assistant Secretary for Energy Efficiency and Renewable Energy, Vehicle Technologies Office, of the U.S. Department of Energy under contract no. DEAC02-05CH11231. The NMR results reported here made use of shared facilities of the UCSB MRSEC (NSF DMR #1720256), a member of the Materials Research Facilities Network (www.mfn.org).

■ REFERENCES

(1) Olivetti, E. A.; Ceder, G.; Gaustad, G. G.; Fu, X. Lithium-ion battery supply chain considerations: analysis of potential bottlenecks in critical metals. *Joule* **2017**, *1*, 229−243.

(2) Meng, Y. S.; Arroyo-de Dompablo, M. E. Recent advances in first principles computational research of cathode materials for lithium-ion batteries. *Acc. Chem. Res.* **2013**, *46*, 1171−1180.

(3) Lee, J.; Urban, A.; Li, X.; Su, D.; Hautier, G.; Ceder, G. Unlocking the potential of cation-disordered oxides for rechargeable lithium batteries. *Science* **2014**, *343*, 519−522.

(4) Clément, R. J.; Lun, Z.; Ceder, G. Cation-disordered rocksalt transition metal oxides and oxyfluorides for high energy lithium-ion cathodes. *Energy Environ. Sci.* **2020**, *13*, 345−373.

(5) Lee, J.; Seo, D.-H.; Balasubramanian, M.; Twu, N.; Li, X.; Ceder, G. A new class of high capacity cation-disordered oxides for rechargeable lithium batteries: Li-Ni-Ti-Mo oxides. *Energy Environ. Sci.* **2015**, *8*, 3255−3265.

(6) Yabuuchi, N.; Takeuchi, M.; Nakayama, M.; Shiiba, H.; Ogawa, M.; Nakayama, K.; Ohta, T.; Endo, D.; Ozaki, T.; Inamasu, T.; Sato, K.; Komaba, S. High-capacity electrode materials for rechargeable lithium batteries: Li3NbO4-based system with cation-disordered rocksalt structure. *Proc. Natl. Acad. Sci. U.S.A.* **2015**, *112*, 7650−7655.

(7) Yabuuchi, N.; Nakayama, M.; Takeuchi, M.; Komaba, S.; Hashimoto, Y.; Mukai, T.; Shiiba, H.; Sato, K.; Kobayashi, Y.; Nakao, A.; Yonemura, M.; Yamanaka, K.; Mitsuhara, K.; Ohta, T. Origin of stabilization and destabilization in solid-state redox reaction of oxide ions for lithium-ion batteries. *Nat. Commun.* **2016**, *7*, 13814.

(8) Chen, D.; Kan, W. H.; Chen, G. Understanding Performance Degradation in Cation-Disordered Rock-Salt Oxide Cathodes. *Adv. Energy Mater.* **2019**, *9*, 1901255.

(9) Lee, J.; Kitchaev, D. A.; Kwon, D.-h.; Lee, C.-w.; Papp, J. K.; Liu, Y.-s.; Lun, Z.; Clément, R. J.; Shi, T.; McCloskey, B. D.; Guo, J.; Balasubramanian, M.; Ceder, G. Reversible Mn2+/Mn4+ double redox in lithium-excess cathode materials. *Nature* **2018**, *556*, 185−190.

(10) Chen, R.; Ren, S.; Knapp, M.; Wang, D.; Witter, R.; Fichtner, M.; Hahn, H. Disordered Lithium-Rich Oxyfluoride as a Stable Host for Enhanced Li + Intercalation Storage. *Adv. Energy Mater.* **2015**, *5*, 1401814.

(11) Ren, S.; Chen, R.; Maawad, E.; Dolotko, O.; Guda, A. A.; Shapovalov, V.; Wang, D.; Hahn, H.; Fichtner, M. Improved Voltage and Cycling for Li + Intercalation in High-Capacity Disordered Oxyfluoride Cathodes. *Adv. Sci.* **2015**, *2*, 1500128.

(12) Baur, C.; et al. Improved cycling stability in high-capacity Li-rich vanadium containing disordered rock salt oxyfluoride cathodes. *J. Mater. Chem. A* **2019**, *7*, 21244−21253.

(13) Lee, J.; Papp, J. K.; Clément, R. J.; Sallis, S.; Kwon, D.-H.; Shi, T.; Yang, W.; McCloskey, B. D.; Ceder, G. Mitigating oxygen loss to improve the cycling performance of high capacity cation-disordered cathode materials. *Nat. Commun.* **2017**, *8*, 981.

(14) Naylor, A. J.; Källquist, I.; Peralta, D.; Martin, J.-F.; Boulineau, A.; Colin, J.-F.; Baur, C.; Chable, J.; Fichtner, M.; Edström, K.; Hahlin, M.; Brandell, D. Stabilization of Li-Rich Disordered Rocksalt Oxyfluoride Cathodes by Particle Surface Modification. *ACS Appl. Energy Mater.* **2020**, *3*, 5937−5948.

(15) Richards, W. D.; Dacek, S. T.; Kitchaev, D. A.; Ceder, G. Fluorination of Lithium-Excess Transition Metal Oxide Cathode Materials. *Adv. Energy Mater.* **2018**, *8*, 1701533.

(16) Clément, R. J.; Kitchaev, D.; Lee, J.; Ceder, G. Short-Range Order and Unusual Modes of Nickel Redox in a Fluorine-Substituted Disordered Rocksalt Oxide Lithium-Ion Cathode. *Chem. Mater.* **2018**, *30*, 6945−6956.

(17) Mozhzhukhina, N.; Kullgren, J.; Baur, C.; Gustafsson, O.; Brant, W. R.; Fichtner, M.; Brandell, D. Short-range ordering in the Li-rich disordered rock salt cathode material Li 2 VO 2 F revealed by Raman spectroscopy. *J. Raman Spectrosc.* **2020**, *51*, 2095−2101.

(18) Lun, Z.; Ouyang, B.; Cai, Z.; Clément, R. J.; Kwon, D.-H.; Huang, J.; Papp, J. K.; Balasubramanian, M.; Tian, Y.; McCloskey, B. D.; Ji, H.; Kim, H.; Kitchaev, D. A.; Ceder, G. Design Principles for High-Capacity Mn-Based Cation-Disordered Rocksalt Cathodes. *Chem.* **2020**, *6*, 153−168.

(19) Ouyang, B.; Artrith, N.; Lun, Z.; Jadidi, Z.; Kitchaev, D. A.; Ji, H.; Urban, A.; Ceder, G. Effect of Fluorination on Lithium Transport

and Short-Range Order in Disordered-Rocksalt-Type Lithium-Ion Battery Cathodes. *Adv. Energy Mater.* **2020**, *10*, 1903240.
(20) Kitchaev, D. A.; Lun, Z.; Richards, W. D.; Ji, H.; Clément, R. J.; Balasubramanian, M.; Kwon, D.-H.; Dai, K.; Papp, J. K.; Lei, T.; McCloskey, B. D.; Yang, W.; Lee, J.; Ceder, G. Design principles for high transition metal capacity in disordered rocksalt Li-ion cathodes. *Energy Environ. Sci.* **2018**, *11*, 2159−2171.
(21) Van der Ven, A.; Aydinol, M. K.; Ceder, G.; Kresse, G.; Hafner, J. First-principles investigation of phase stability in Li_xCoO_2. *Phys. Rev. B: Condens. Matter Mater. Phys.* **1998**, *58*, 2975.
(22) Tepesch, P. D.; Garbulsky, G. D.; Ceder, G. Model for Configurational Thermodynamics in Ionic Systems. *Phys. Rev. Lett.* **1995**, *74*, 2272−2275.
(23) Walle, A.; Ceder, G. Automating first-principles phase diagram calculations. *J. Phase Equilib.* **2002**, *23*, 348−359.
(24) Nelson, L. J.; Hart, G. L. W.; Zhou, F.; Ozoliņš, V. Compressive sensing as a paradigm for building physics models. *Phys. Rev. B: Condens. Matter Mater. Phys.* **2013**, *87*, 035125.
(25) Kresse, G.; Furthmüller, J. Efficiency of ab-initio total energy calculations for metals and semiconductors using a plane-wave basis set. *Comput. Mater. Sci.* **1996**, *6*, 15−50.
(26) Kresse, G.; Joubert, D. From ultrasoft pseudopotentials to the projector augmented-wave method. *Phys. Rev. B: Condens. Matter Mater. Phys.* **1999**, *59*, 1758.
(27) Perdew, J. P.; Burke, K.; Ernzerhof, M. Generalized gradient approximation made simple. *Phys. Rev. Lett.* **1996**, *77*, 3865−3868.
(28) Wang, L.; Maxisch, T.; Ceder, G. Oxidation energies of transition metal oxides within the GGA+U framework. *Phys. Rev. B: Condens. Matter Mater. Phys.* **2006**, *73*, 195107.
(29) Jain, A.; Hautier, G.; Ong, S. P.; Moore, C. J.; Fischer, C. C.; Persson, K. A.; Ceder, G. Formation enthalpies by mixing GGA and GGA + U calculations. *Phys. Rev. B: Condens. Matter Mater. Phys.* **2011**, *84*, 045115.
(30) O'Dell, L. A.; Rossini, A. J.; Schurko, R. W. Acquisition of ultra-wideline NMR spectra from quadrupolar nuclei by frequency stepped WURST−QCPMG. *Chem. Phys. Lett.* **2009**, *468*, 330−335.
(31) Pell, A. J.; Clément, R. J.; Grey, C. P.; Emsley, L.; Pintacuda, G. Frequency-stepped acquisition in nuclear magnetic resonance spectroscopy under magic angle spinning. *J. Chem. Phys.* **2013**, *138*, 114201.
(32) Sananes, M. T.; Tuel, A.; Hutchings, G. J.; Volta, J. C. Characterization of Different Precursors and Activated Vanadium Phosphate Catalysis by 31P NMR Spin Echo Mapping. *J. Catal.* **1994**, *148*, 395−398.
(33) Massiot, D.; Farnan, I.; Gautier, N.; Trumeau, D.; Trokiner, A.; Coutures, J. P. 71Ga and 69Ga nuclear magnetic resonance study of β-Ga2O3: resolution of four-and six-fold coordinated Ga sites in static conditions. *Solid State Nucl. Magn. Reson.* **1995**, *4*, 241−248.
(34) Jain, A.; Ong, S. P.; Hautier, G.; Chen, W.; Richards, W. D.; Dacek, S.; Cholia, S.; Gunter, D.; Skinner, D.; Ceder, G.; Persson, K. a. The Materials Project: A materials genome approach to accelerating materials innovation. *APL Mater.* **2013**, *1*, 011002.
(35) Hume-Rothery, W.; Powel, H. M. On the Theory of Super-Lattice Structures in Alloys. *Z. Kristallogr. - Cryst. Mater.* **1935**, *91*, 23−47.
(36) Shannon, R. D. Revised effective ionic radii and systematic studies of interatomic distances in halides and chalcogenides. *Acta Crystallogr., Sect. A: Cryst. Phys., Diffr., Theor. Gen. Crystallogr.* **1976**, *32*, 751−767.
(37) Urban, A.; Abdellahi, A.; Dacek, S.; Artrith, N.; Ceder, G. Electronic-Structure Origin of Cation Disorder in Transition-Metal Oxides. *Phys. Rev. Lett.* **2017**, *119*, 176402.
(38) Chen, D.; Wu, J.; Papp, J. K.; McCloskey, B. D.; Yang, W.; Chen, G. Role of Redox-Inactive Transition-Metals in the Behavior of Cation-Disordered Rocksalt Cathodes. *Small* **2020**, *16*, 2000656.
(39) Ji, H.; Urban, A.; Kitchaev, D. A.; Kwon, D.-H.; Artrith, N.; Ophus, C.; Huang, W.; Cai, Z.; Shi, T.; Kim, J. C.; Kim, H.; Ceder, G. Hidden structural and chemical order controls lithium transport in cation-disordered oxides for rechargeable batteries. *Nat. Commun.* **2019**, *10*, 592.
(40) Lun, Z.; Ouyang, B.; Kitchaev, D. A.; Clément, R. J.; Papp, J. K.; Balasubramanian, M.; Tian, Y.; Lei, T.; Shi, T.; McCloskey, B. D.; Lee, J.; Ceder, G. Improved Cycling Performance of Li-Excess Cation-Disordered Cathode Materials upon Fluorine Substitution. *Adv. Energy Mater.* **2019**, *9*, 1802959.
(41) Ji, H.; Kitchaev, D. A.; Lun, Z.; Kim, H.; Foley, E.; Kwon, D.-H.; Tian, Y.; Balasubramanian, M.; Bianchini, M.; Cai, Z.; Clément, R. J.; Kim, J. C.; Ceder, G. Computational Investigation and Experimental Realization of Disordered High-Capacity Li-Ion Cathodes Based on Ni Redox. *Chem. Mater.* **2019**, *31*, 2431−2442.
(42) House, R. A.; Jin, L.; Maitra, U.; Tsuruta, K.; Somerville, J. W.; Förstermann, D. P.; Massel, F.; Duda, L.; Roberts, M. R.; Bruce, P. G. Lithium manganese oxyfluoride as a new cathode material exhibiting oxygen redox. *Energy Environ. Sci.* **2018**, *11*, 926−932.
(43) Kataoka, R.; Kojima, T.; Takeichi, N. Electrochemical property of Li-Mn cation disordered Li-rich Li2MnO3 with nacl type structure. *J. Electrochem. Soc.* **2018**, *165*, A291.
(44) Seo, D.-H.; Lee, J.; Urban, A.; Malik, R.; Kang, S.; Ceder, G. The structural and chemical origin of the oxygen redox activity in layered and cation-disordered Li-excess cathode materials. *Nat. Chem.* **2016**, *8*, 692−697.
(45) Ji, H.; et al. Ultrahigh power and energy density in partially ordered lithium-ion cathode materials. *Nat. Energy* **2020**, *5*, 213−221.

https://dx.doi.org/10.1021/acs.chemmater.0c04109
Chem. Mater. XXXX, XXX, XXX−XXX